Multidimensional excitation pulses based on spatiotemporal encoding concepts

Jean-Nicolas Dumez, Lucio Frydman *

Department of Chemical Physics, Weizmann Institute of Science, Rehovot 76100, Israel

ARTICLE INFO

ABSTRACT

The understanding and control of spin dynamics play a fundamental role in modern NMR imaging, for devising new ways to monitor an object's density as well as for enabling the tailored excitation of spins in space. It has recently been shown that by relying on spatiotemporal encoding (SPEN), new forms of single-scan multidimensional NMR spectroscopy and imaging become feasible. The present study extends those imaging developments, by introducing a new class of multidimensional excitation pulses that relies on SPEN concepts. We focus in particular on a family of "hybrid" 2D radiofrequency (RF) pulses that operate in both direct and reciprocal excitation space, and which can spatially sculpt the spin magnetization in manners that are beyond the reach of sequential 1D pulse shaping. These SPEN-based 2D pulses are compatible with a majority of single- and multi-scan imaging techniques. Like the corresponding SPEN-based hybrid 2D acquisitions, these pulses can benefit from a high robustness against field inhomogeneities and/or offset effects that affect their k-space-based counterparts. These properties are analyzed, and illustrated with numerical simulations and model experiments.

1. Introduction

Selective pulses play numerous roles in nuclear magnetic resonance (NMR). In spectroscopy they help simplify the information content and can increase sensitivity [1,2]. In NMR imaging (MRI) they are widely used to limit the extent of the spatial region from which the observed NMR signals originate [3]; for similar reasons they are integral component of spatially localized *in vivo* spectroscopic measurements [4]. All such experiments usually seek to delineate a slice or a voxel in space, and utilize for this selective RF pulses applied in the presence of magnetic field gradients. Each pulse will then address selectively a slab within the sample, leading to slice-, line- or cube-shaped spatial excitations. In many instances, however, more complex 2D or 3D regions of interest (ROIs) are sought. These may attempt targeting the shape of a particular organ [5–7], exciting selected chemical components with a pre-defined spatial location within the sample [8,9], or endowing complex geometries with pre-set excitation phases that compensate for magnetic field inhomogeneities [10–12]. Such multidimensional spatial or spectral–spatial selectivity often requires more sophisticated strategies than what can be achieved within the

context of simple 1D frequency-selective pulses; they call for the use of so-called multidimensional RF schemes [13–15].

An essential component in the design of frequency-selective pulses in one or more dimensions is the Fourier relationship that, in the limit of small excitation angles, relates a time-dependent B_1 field with the spectral distribution excited as a function of frequency [2]. Walks in reciprocal spaces enable an extension of this and other classic RF selectivity concepts, from one to multiple dimensions. These "excitation k-spaces" [14] provide a unified description relating the shape of the RF waveform as a function of time, with the properties that can be excited from the spins along n spatial dimensions. Most modern multidimensional pulse-design approaches build upon this excitation k-space [16,17], and its associated Fourier properties. Also built around Fourier-based k-space concepts is the contemporary explanation of a majority of MRI experiments [18,19]. Walks through k-space, for instance, underlie the operation of echo-planar imaging (EPI) approaches capable of delivering multidimensional spatial profiles in a single-scan. Although a majority of single-scan MRI experiments exploit such k-space concepts to define the features that will characterize the image being sought [3], a number of alternatives to EPI exist in ultrafast multidimensional MRI [20–25]. Owing to their ability to probe the spin response throughout a multidimensional space in a single scan, these alternatives might also constitute a basis for the design of multidimensional spatial or spatial/spectral excitation pulses. One such non-EPI scanning method, dubbed spatiotemporal encoding (SPEN), relies on measuring the NMR signal in "direct" rather than in reciprocal space. SPEN

---

operates by generating a spin response that at any given instant throughout the signal acquisition carries only contributions from a very localized region of the sample. This approach has been shown to benefit from robustness against the effect of undesirable frequency offsets – arising, for example, from chemical shifts or magnetic susceptibility differences [26].

In this article, we demonstrate that spatiotemporal-encoding concepts can lead to a novel class of multidimensional pulses, the operation of which is distinct from that of *k*-space-based pulses. This demonstration proceeds in two stages. We begin with a description of how a spatiotemporal, sequential excitation of arbitrary 1D spin profiles can be imparted in both continuous and discrete manners. We then consider 2D analyses focusing on a number of options, and in particular on a "hybrid" 2D approach whereby spins are excited along one spatial dimension based on discretized SPEN concepts and along an orthogonal dimension based on standard *k*-space approaches. Both calculations and experiments demonstrate that the ensuing pulses, which can be

seen as operating in both direct and reciprocal spaces, are compatible with SPEN-based as well as with conventional *k*-space-based NMR imaging. In the latter, more usual case, attention is placed on a self-unfolding property of these new pulses that endows them with a high robustness against field inhomogeneities and/or chemical shift offsets.

2. Theory

2.1. RF spatial sculpting using SPEN concepts in one dimension

NMR imparts 1D spatial selectivity by applying a shaped RF waveform in unison with an external magnetic field gradient. In typical excitation schemes RF pulses address all the frequency elements within a targeted ROI simultaneously; in SPEN-oriented excitation pulses, spins across the sample will be addressed sequentially by the combined action of the magnetic field gradient and of a frequency-swept RF. In the simplest description of these
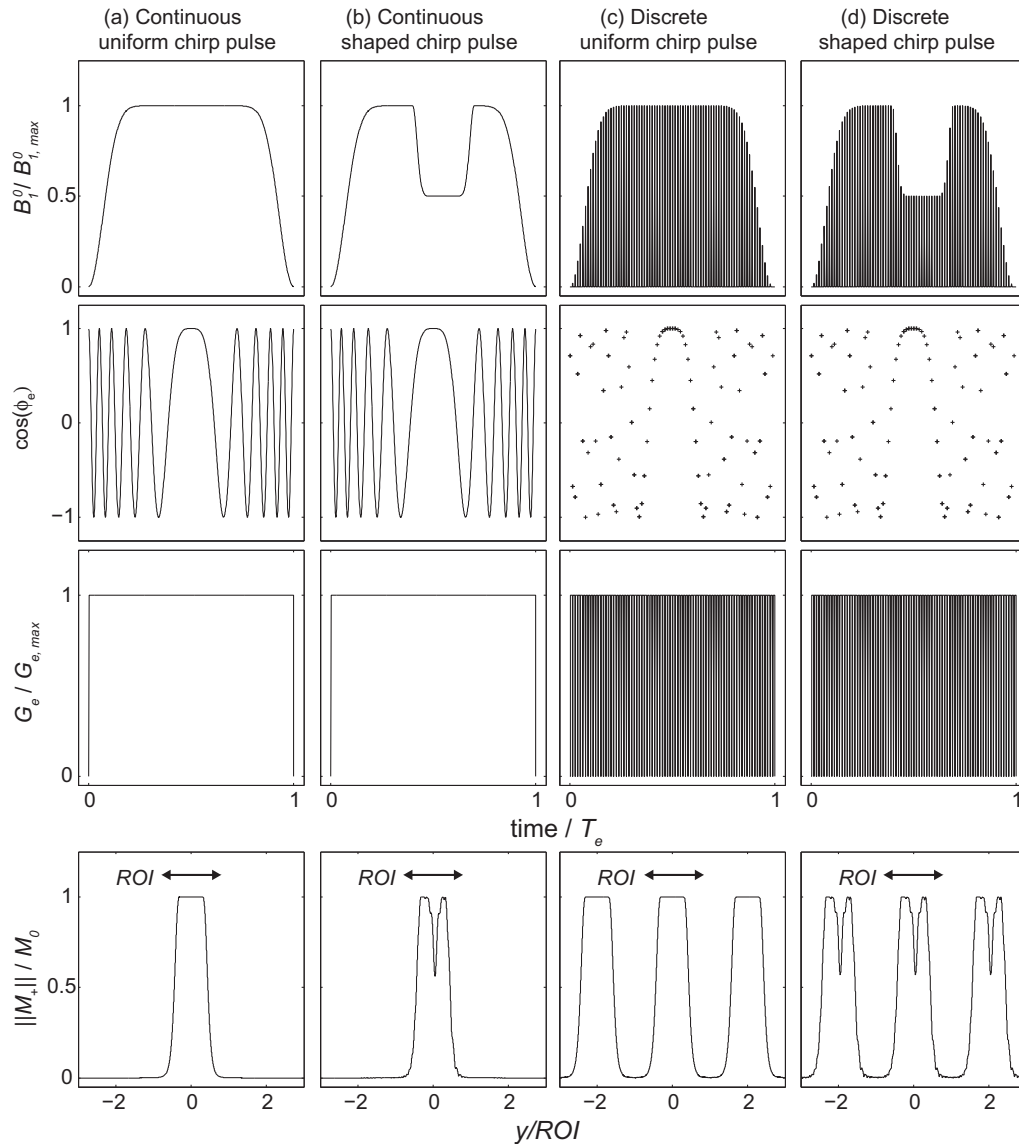
Fig. 1. One-dimensional excitation in direct space using a linearly frequency-swept pulse. Examples are given for a region of interest of length ROI, indicated by a double arrow, and of uniform (a and c) or shaped (b and d) amplitude, excited using either a continuous (a and b) or a discretized (c and d) pulse. In each case, the RF amplitude, the RF phase and the gradient amplitude are shown in the first, second and third row respectively. The magnitudes of the transverse magnetization at the end of the pulse, calculated using Bloch simulations, are shown in the fourth row. The time-bandwidth product of the pulses are $Q = 40$ for all cases; the discretized pulses use $N_e = 80$ steps, resulting in the excitation of periodic sidebands with a replication length of (N_e/Q)ROI = 2ROI.

pulses spins are acted upon instantaneously when the carrier frequency of a linearly-swept (chirped) RF matches their resonance frequency, and precess freely otherwise [27]. When a constant-amplitude profile is used the ensuing RF waveform can be written in the usual rotating frame:

$$B_1(t) = B_1^0 \exp\left[i\left(O_{i,e}t + \frac{R_e t^2}{2} + \phi_0\right)\right] = B_1^0 \exp[i\phi_e], \quad (1)$$

where B_1^0, ϕ_0, R_e and $O_{i,e}$ are the RF amplitude, an arbitrary initial phase (set henceforth to zero), the constant sweep rate and the initial carrier frequency offset of the excitation pulse, respectively. This approach leads to a uniform excitation of an initially longitudinal magnetization $\mathbf{M_z}$, into a post-excitation transverse magnetization $\|\mathbf{M_+}\|$. The effective nutation angle $0 \leqslant \theta \leqslant \pi$ associated to this sweep can be set according to the B_1^0 value chosen, and the post-excitation phase of the spins can be well approximated by the quadratic form [27–31]:

$$\phi_{exc}(y) = \left(-\frac{(\gamma G_e)^2}{2R_e}\right)y^2 + \left(\gamma G_e\left(T_e + \frac{O_{i,e} - \Omega}{R_e}\right)\right)y$$
$$+ \left(\Omega T_e - \frac{(O_{i,e} - \Omega)^2}{2R_e} - \frac{\pi}{2}\right), \quad (2)$$

where G_e is the amplitude of a gradient assumed applied along the $\hat{y}$-axis, T_e is the overall duration of the pulse, and Ω is a site-specific frequency offset associated to chemical shift or field inhomogeneity effects. In practice, the amplitude modulation of the frequency-swept pulse is not strictly constant, as some smoothing is usually applied to avoid the ringing induced by the finite duration of the pulse [32,33]. Such smoothing of the waveform can be achieved with a WURST-like envelope [33], transitioning outside the targeted ROI and leaving the excitation phase in Eq. (2) virtually unchanged. If the effects of the *a priori* unknown offset Ω can be disregarded (or if its value as a function of $\hat{y}$ is known, cf. Refs. [24,26]) the excitation of a sculpted $\|\mathbf{M_+}\|(y)$ is straightforward, simply by imparting a time-dependency $B_1^0(t)$ to the amplitude of the chirp pulse as the RF addresses various y-dependent positions, as illustrated in Fig. 1a and b. At times t this pulse will impart on the corresponding $y(t)$

$$y(t) = \frac{(O_{i,e} - \Omega) + R_e t}{\gamma G_e}, \quad (3)$$

a nutation angle $\theta(t)$, depending on the shape given to B_1^0.

Whereas continuous versions of these frequency-swept pulses can impart nearly ideal profiles, various properties of the multidimensional schemes described below will require considering the behavior of these RF pulses upon discretization. Discretization is nowadays an inherent feature of any shaped RF pulse, dictated by hardware-based shaping constraints. What we consider here, however, are the particular effects that arise upon replacing the finely modulated RF pulse acting in the presence of a constant gradient, by an alternation of N_e square pulses acting in the absence of gradients interleaved with N_e gradient "blips" acting on freely evolving spins between the pulses. Both of these events are therefore clocked out at a common rate $\Delta t^{-1} = N_e/T_e$. The integrated area and the phase of the jth square pulse will be given by $B_1^0(t_j)T_e/N_e$ and ϕ_j, respectively, where $t_j = j\Delta t$; and the blipped gradients will be assumed identical and square with integrated areas $\Delta k_e \approx (\gamma G_e T_e)/N_e$ each. Fig. 1c and d illustrates this discretization process as well as its effects on the ensuing sculpting. The main consequence of this discretization is the periodic replication of the excited magnetization profile, as can be seen by comparison against Fig. 1a and b. These replicas become increasingly closer as the number of N_e events decreases. This effect reflects the fact that any two spin-packets for which the gradient-derived precession phase varies by a multiple of 2π in any given Δt step will appear indistinguishable when acted upon by the subsequent RF pulse. Notice that in contrast to traditional DANTE [34] or to "gapped" [35] pulses, the precession and nutation steps are entirely separated in the implementation just described; this is similar to what has been recently described in the PINS approach [36], and explains the identical intensities elicited (at least in such fully broadband simulations unaffected by instrumental limitations) by all excitation center-/side-bands.

Fig. 2 expands on another aspect of the magnetization profile that will be excited by a discretized chirp pulse: as predicted for the continuously swept case (Eq. (2)) this excitation will also in this case impart an approximately quadratic phase profile for the transverse magnetization – not only for the centerband being addressed, but also for the excitation sidebands that flank it. Assuming for simplicity that these excitation sidebands fall outside the targeted ROI and can thereby be ignored, the originating signal would still be ready for SPEN-based MRI but not in general for conventional k-space-based acquisitions. Indeed, signals in SPEN experiments originate from points of the sample that correspond to an extremum of the spatially varying parabolic phase [22–24,28]; this "stationary point" will move as an acquisition gradient G_a is applied, rasterizing the response of the full sample as the acquisition time reaches $T_a = |G_e T_e/G_a|$. By contrast, the parabolic phase associated to a continuous or discretized chirp pulse is not suitable in general for a Fourier-based MRI. Fourier transformation of the signal acquired from a magnetization with a quadratic-phase, a so-called "pseudo-echo" [37], will only yield an image without aliasing if the quadratic phase does not involve frequencies larger than $\gamma G_a FOV$, where G_a is the acquisition gradient and *FOV* the field of view [37]. A simple strategy for removing this quadratic phase imparted by an excitation chirp pulse – while preserving its B_1^0-imparted profile – consists of following the excitation by a suitably defined frequency-swept refocusing pulse [28–30,32]. Pairs of frequency-swept pulses are frequently used for volume selection in localized spectroscopy [38]; generalized hyperbolic secant and adiabatic SLR pulses have also been paired to perform slice selection in imaging experiments [39,40]. The phase accrued after applying such an adiabatic 180° swept pulse can be written as [28]:

$$\phi_{ref}(y) = -\phi_{exc}(y) + \left(-\frac{(\gamma G_r)^2}{R_r}\right)y^2 + \left(\gamma G_r\left(T_r + \frac{2(O_{i,r} - \Omega)}{R_r}\right)\right)y$$
$$+ \left(\Omega T_r - \frac{(O_{i,r} - \Omega)^2}{R_r}\right), \quad (4)$$

where T_r, R_r, $O_{i,r}$ and G_r are, respectively, the duration, the sweep rate, the initial carrier frequency and the concurrent gradient associated with the 180° refocusing pulse; ϕ_{exc} is an initial phase given by either Eq. (2) or by a "discretized" version of thereof. For simplicity, we shall assume here that the refocusing pulse is always played out continuously. When this refocusing chirp pulse follows the excitation chirp pulse and addresses the same region of interest, setting $T_e G_e = 2T_r G_r$ will entirely remove the quadratic phase dependence of the ϕ_{ref} in Eq. (4). In particular, Fig. 2 demonstrates how the simple choice of parameters $T_e = 2T_r$ and $G_e = G_r$ succeeds in removing the contribution of the quadratic phase off the targeted ROI, which therefore ends up ready to be analyzed by conventional k-space Fourier imaging. Notice as well that as a result of the double-sweep: (i) the linear phase contribution previously arising from the chemical shifts is removed; (ii) if/when using a discretized version of the 90° chirp pulse, the quadratic phase contributions that previously affected the excitation sidebands will be removed by the 180° post-excitation adiabatic sweep only for the fraction of the sidebands that is swept over by the refocusing pulse.
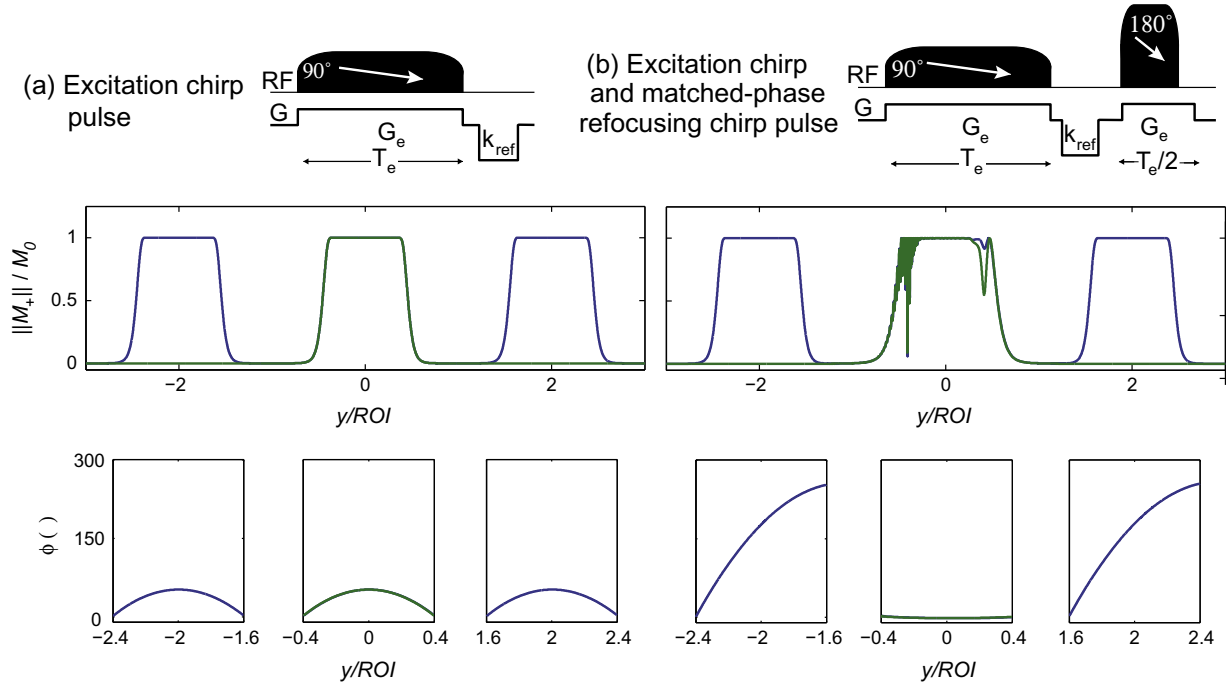
Fig. 2. Bloch-simulations of the transverse magnetizations excited by a chirp pulse (a), and by the combination of excitation and refocusing chirp pulses (b). Pulse sequences are shown in the first row; the magnitude and phase of the transverse magnetization are shown in the second and third row, respectively. The excitation chirp pulse has a time-bandwidth product $Q = 100$ and is assumed either continuous (green traces) or discretized with $N_e = 200$ steps (blue). Notice that discretization results in the excitation of periodic sidebands with a replication length of (N_e/Q)ROI = 2ROI. The two pulses are assumed applied under identical gradient amplitudes and sweep over identical regions of length ROI. The duration of the (continuous) refocusing chirp pulse is half that of the excitation chirp pulse, so as to cancel the quadratic phase of the centerband at its conclusion. An additional gradient lobe of area $k_{ref} = -G_e T_e/2$ is inserted to cancel the linear phase of the centerband. The distortions of the ROI in (b) corresponds to the transition regions of the refocusing pulse, and their unwanted contributions to the signal can be suppressed with crusher gradients. (For interpretation of the references to color in this figure legend, the reader is referred to the web version of this article.)

2.2. Discretized SPEN-based RF pulses: dealing with excitation sidebands

The existence of excitation sidebands can have important consequences. In usual experiments the MRI signal to be acquired should originate only from the targeted region of interest; i.e., from the centerband. For either k-space-based or SPEN-based MRI experiments, the signal eventually detected after a discretized excitation can in principle include contributions arising from undesirable excitation sidebands. One possibility to overcome this problem is to presaturate potential sources of interference arising from voxels outside the ROI. Alternatives include designing the discretized pulse so that its excitation sidebands fall outside the sample, or applying a refocusing pulse selectively on the centerband. All such approaches are of common use, particularly when dealing with multidimensional RF pulse designs that often rely on discretization along only one of the sample's axes [16,41]. Requesting that the excitation sidebands fall outside a pre-defined ROI sets bounds on the properties of the discretized RF pulse and of its associated gradient. For the SPEN-based pulses considered here, a given chirp excitation bandwidth $\Delta v = (O_{f,e} - O_{i,e})/2\pi$ will define the ROI as $2\pi\Delta v/\gamma G_e$. The separation ΔL at which the excitation sideband will appear replicated can in turn can be related to the interval $\Delta t = T_e/N_e$ that separates the subpulses of the discretized chirp pulse, according to $\gamma G_e \Delta L = 2\pi/\Delta t$. The condition for the excitation sidebands to appear clearly separated from the centerband is thus $\Delta L > $ ROI, or alternatively

$$\frac{N_e}{\Delta v \cdot T_e} > 1 \Longleftrightarrow N_e > Q = \Delta v \cdot T_e. \tag{5}$$

Eq. (5) states that the number of subpulses in the discretized pulse should be larger than the time-bandwidth product $Q = \Delta v \cdot T_e$ pulse. This time-bandwidth product is a dimensionless measure of

the pulse's performance: for a chirp pulse, the selectivity of the pulse improves as Q increases. Also the curvature of the quadratic-phase parabola imprinted on the spins by a swept pulse is proportional to Q. In SPEN experiments time-bandwidth products in the 50–100 range are not unusual; such a high number of discretized subpulses may not be realistic in most multidimensional pulse contexts. Lower Q values can often be tolerated, although if $Q < 20$ the assumption of a progressive excitation underlying the use of chirped excitations begins to break down. It is also worth pointing out that although low Q values were a limitation in the original implementation of spatiotemporal encoding [22–24], improved reconstruction schemes now make it possible to recover a spatial resolution that is given by the number of acquired points rather than $\sqrt{Q}$ [42].

As mentioned above, the main complication associated with excitation sidebands arises when one cannot avoid their overlapping with the central ROI being targeted. One possibility to circumvent these limitations without employing an inordinately high number of N_e steps or very long pulse lengths T_e, is by reducing the chirped bandwidth Δv. For a given ROI Eq. (5) indicates that this can be achieved by reducing the associated gradient amplitude G_e such that

$$G < \frac{2\pi N_e}{\gamma \text{ROI} \cdot T_e}. \tag{6}$$

Similar bounds on the gradient amplitude are known for the case of Fourier-based discrete pulses [16], and like in those instances their adoption poses a problem: weakening gradients as demanded by Eq. (6) may make the pulse susceptible to distortions, particularly those arising from susceptibility and chemical-shift effects. These effects become secondary if strong gradients can be used; in the case of k-space-based pulses, it is possible to

deal with the ensuing sideband/centerband overlaps that then arise by performing multiple acquisitions, which are combined to recover a centerband-only signal [6,43].

For discretized SPEN pulses, the contribution of the centerband and the sidebands can under certain conditions be separated in a single conventional scan – even when dealing with cases of significant overlap. This in turn opens the possibility to use intense gradients, endowing the ensuing SPEN-based strategy with high immunity against undesirable frequency offsets. This will be a meaningful consideration in the design of 2D pulses, and therefore it is convenient to consider its physical basis for the simpler one-dimensional cases. Under the effects of a discretized excitation, the total magnetization excited by a pulse can be quite complex. A substantial simplification results if the flip angle remains small enough for all positions. In such instances the total magnetization is conveniently described as a sum over bands:

$$\mathbf{M}(y) = \sum_p \mathbf{M}_p(y), \qquad (7)$$

where for simplicity the index $p = 0$ denotes the centerband; i.e., the ROI being sought. In practice the sum could be restricted to bands that fall within the sample. Owing to the small-flip-angle assumption, the excited magnetization will still be linear with respect to B_1 even if the various excited bands overlap. Amplitude-wise the sideband intensities will then be identical replica of the centerband; phase-wise they will fulfill the condition

$$\mathbf{M}_p(y + p \cdot \Delta L) = |\mathbf{M}_o(y)| \cdot \exp\left\{ i\left[\phi_o(y) + p\left(\frac{(\gamma G_e)^2}{R_e}\Delta L\right)y \right] \right\}, \qquad (8)$$

where $\phi_o(y)$ is as given in Eq. (2), all remaining parameters are as described earlier, and constant phase terms have been disregarded. Eq. (8) highlights the fact that, while all bands share an identical
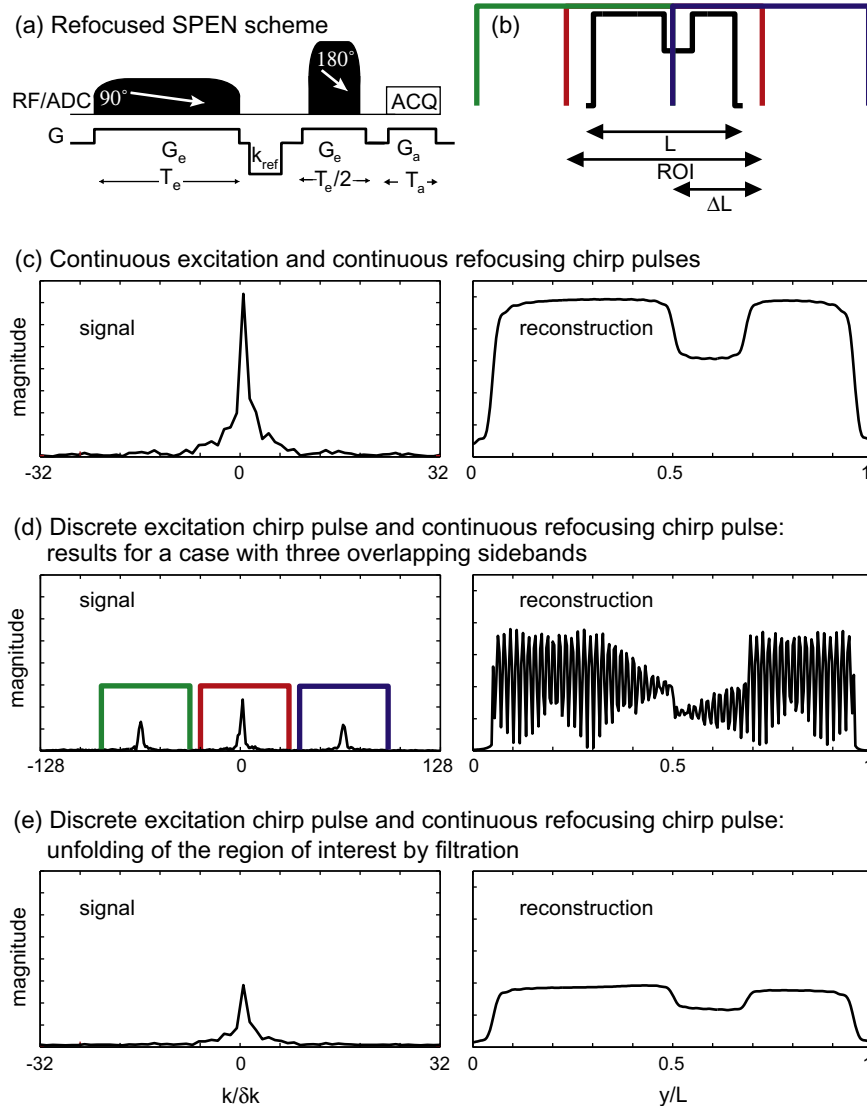

Fig. 3. Strategy to separate the excitation center- and side-bands arising upon using discrete excitation and continuous refocusing chirped pulse, illustrated with Bloch simulations. The pulse sequence assumes a 1D spin-echo MRI experiment involving a discretized version of the 90° chirp pulse/gradients shown in (a), and is assumed to image a phantom of size L shown in black in (b). The discrete excitation chirp pulse has a time-bandwidth product $Q = 200$. The two pulses are played with the same gradient amplitude and sweep over the same region of interest of length ROI = 1.5L. The duration of the refocusing chirp pulse is half that of the excitation chirp pulse, such that the quadratic phase of the centerband is cancelled at the end of the refocusing pulse. The signal and its Fourier transform (FT) are shown in (c) for a continuous excitation chirp pulse, illustrating the feasibility of Fourier imaging after such a pair of chirp pulses. The signal and FT shown in (d) correspond to an excitation chirp pulse discretized with $N_e = 100$ steps. As the amplitude of the discretized excitation chirp pulse is chosen such that it is in the linear regime, each echo in (d) corresponds to a band excited by the discretized chirp pulse, as indicated by the colored regions shown in (b and d). In (e), the central echo of the signal shown boxed in red in (d), consisting of $64 \simeq N_e * (L/\text{ROI})$ points filtered from the full signal, and its Fourier transform illustrate how the image of the ROI can be recovered despite the fact that excitation sidebands overlap with the centerband. (For interpretation of the references to color in this figure legend, the reader is referred to the web version of this article.)

quadratic contribution in their phases, they do differ by a linear phase coefficient. This allows one to separate the contribution of the centerband to the signal from that of the sidebands: if, following the excitation process, the quadratic phase terms are removed (for instance by the application of a suitable 180° adiabatic chirp pulse as explained earlier) each band will then form its own individual echo at a distinct location in k-space. Fig. 3 illustrates a way of achieving and exploiting this, for the case of overlapping bands arising due to a discrete excitation that breaks the $G < \frac{2\pi N_e}{\gamma \text{ROI} \cdot T_e}$ condition given in Eq. (6) (i.e., for a case where the centerband and the sidebands overlap). In this example the post-excitation 180° refocusing pulse removed the quadratic phase for the center- and for the overlapping side-bands; as per Eq. (8), these bands will still differ from one another by a linear term of the form $p\left(\frac{(\gamma G_e)^2}{R_e} \Delta L\right)y = pN_e\left(\frac{y}{\text{ROI}}\right)$. As a result of this difference a linear gradient applied before or after the refocusing pulse will lead to a distinct echo for each band; the contribution of the centerband can thus be retrieved by a simple k-domain weighting fashion, despite the fact that its spectrum overlaps with that of the sidebands. Notice that this approach provides a way to increase the gradient amplitude G_e associated with the spatial selectivity and thus to improve the robustness of the RF pulse against field inhomogeneities. This improvement, however, comes at a price in sensitivity: preserving the linear approximation implicit in Eq. (7) implies that only a fraction of the magnetization in the ROI being excited, corresponds to the undistorted centerband being sought. The remaining portion of the magnetization corresponds to harmonics of the excitation sidebands, that overlap with the centerband and whose imaging information is not faithful.

2.3. Spatial sculpting using SPEN-based RF pulses: multiple dimensions

The analysis just outlined for a 1D scenario can be generalized in different manners to the sculpting of magnetizations in two or more spatial dimensions. It is arguably easiest to consider first a "hybrid" scenario, whereby the frequency-swept SPEN-based strategy is used to shape the spatial profile along one dimension, while a conventional Fourier-based analysis imparts the excitation shape being sought along an orthogonal dimension. Such a hybrid direct-plus-reciprocal excitation space can, for example, be explored using the blipped Cartesian trajectory illustrated in Fig. 4a, where the SPEN dimension is the y spatial axis and the Fourier dimension is x. In practice, and in the spirit of conceptually similar single-scan 2D "hybrid" imaging experiments [23,24], a chirped-like SPEN encoding like the one described in the previous Section is implemented along the "slow" (low-bandwidth) dimension in a discrete manner, while a k-space Fourier-designed waveform is used to impart spatial selectivity along the second, "fast" (high-bandwidth) dimension. An illustrative waveform is shown in Fig. 4b, where all the subpulses were chosen as identical $sinc$ pulses, with an overall phase and amplitude modulation of the pulse train that corresponds to a discrete, linear frequency-sweep. Such an approach is akin to the "separable" design originally introduced to obtain adiabatic 2D pulses [44], which has also been used to develop other families of pulses based on an echo-planar trajectory, the so-called "echo-planar pulses" [45,46]. Following the model of Ref. [44], the alternating polarity of the "fast" gradient for even and odd subpulses makes each pulse inherently refocused; the 2D pulse thus behaves in the slow dimension as if its constituent subpulses were square pulses. This enables a considerable simplification in the design of the pulse-driven magnetization sculpting, as the shapes to be imparted along the two dimensions can be treated independently. Notice that since the 2D pulse introduced here can be seen as operating in a hybrid direct (y) and in a reciprocal (k_x) space, it stands by contrast to Fourier 2D pulses which operate entirely in a 2D reciprocal space.
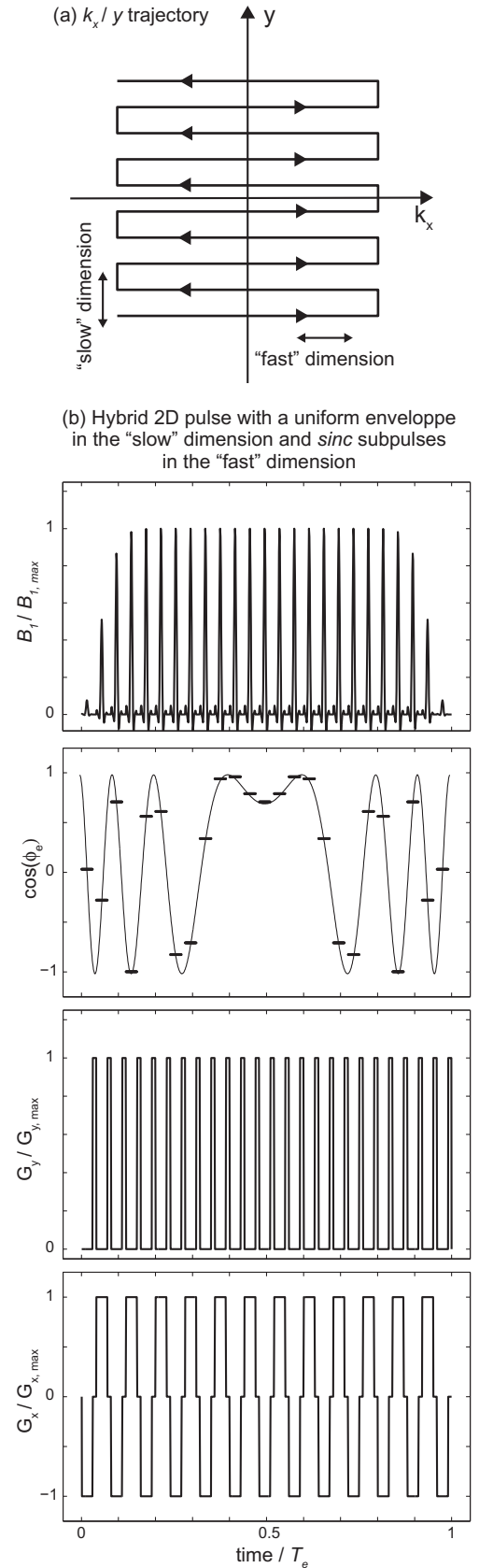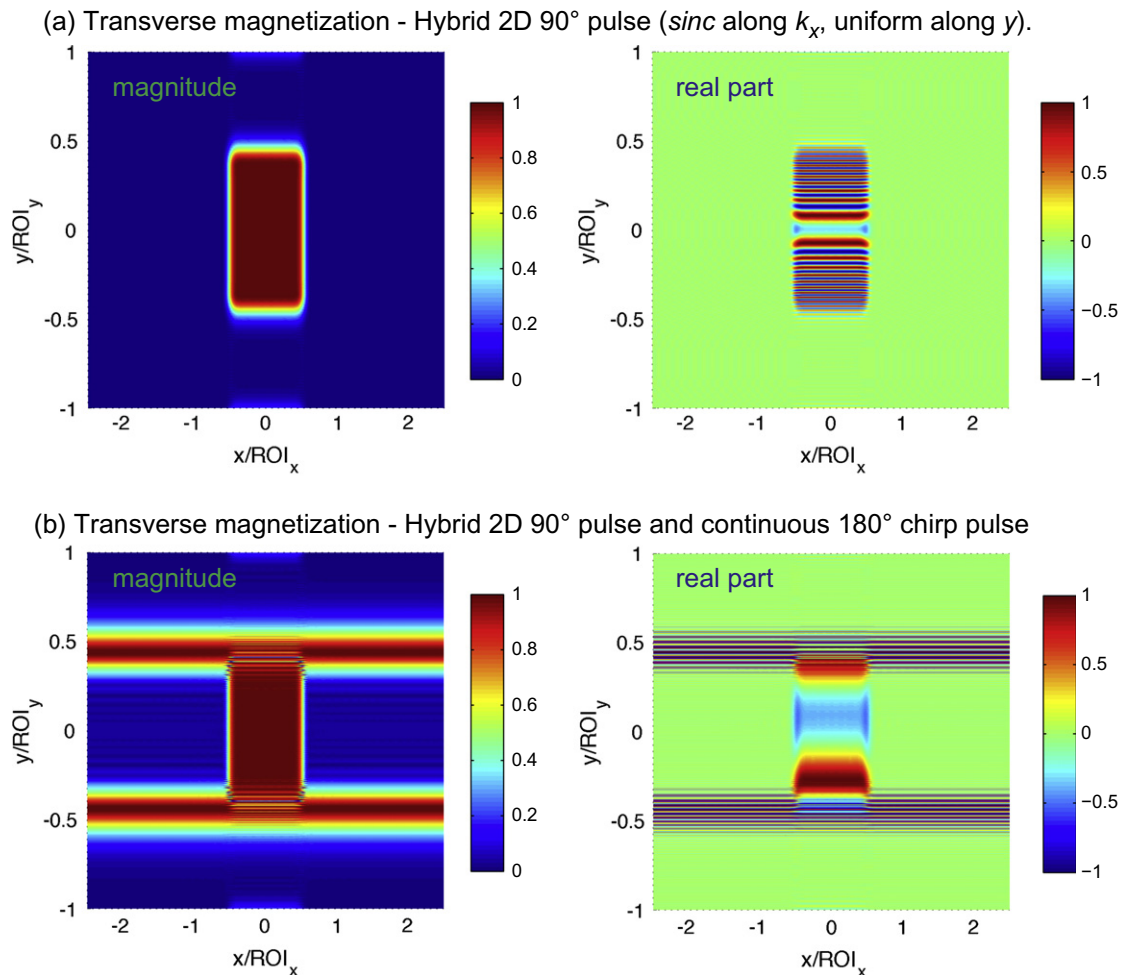

Fig. 4. (a) Trajectory in excitation space for a hybrid 2D pulse, where spins are excited sequentially along the "slow" dimension (y), while k-space is used along the "fast" dimension (k_x). (b) RF and gradient waveform details for a hybrid y/k_x 2D excitation pulse with $N_e = 25$ subpulses. A thin line shows the original continuous modulation of ϕ_e, sampled here with N_e discrete steps.

Fig. 5 shows numerical examples of magnetization excited with the aid of such a hybrid 2D pulse. Fig. 5a shows a simple case where a finely digitized pulse acted uniformly along the slow dimension, imprinting a quadratic phase of the kind usually desired in SPEN imaging. In the fast dimension, all the subpulses were imparted as k-domain $sinc$ shapes, leading the excitation of a slab of width ROI_x along this dimension. Fig. 5b shows a variation of this excitation mode, incorporating a 180° sweep following the 2D hybrid excitation. As discussed in detail for the 1D case, suitable timing of this adiabatic sweep can remove the quadratic phase dependence and enable conventional imaging. As in the 1D case, multiple sidebands will be generated when using a coarser increment for the SPEN modulations – coarser either because of an increase in the time step intervals or due to a reliance on a bigger G_e gradient. Once again, the excitation replicas arising along the "slow" dimension can be separated and filtered out by tailoring the 180° adiabatic refocusing conditions.

In addition to the option of imparting 2D spatial selectivity using a sequential, SPEN-based excitation of the spins along one dimension and a k-space-based tailoring of the pulse along an orthogonal axis, it is worth considering the use of a purely SPEN-based strategy. Such an approach would impart a 2D excitation shape by performing a time-incremented, sequential excitation of the spins along a pre-defined 2D spatial trajectory. It is conceivable that some of the benefits noted upon using SPEN-sculpting in 1D, such as the possibility to actively compensate for field inhomogeneities in a voxel-by-voxel manner [24], could be extended in this fashion to a higher-dimensional space. Fig. 6 explores two possibilities to obtain such purely SPEN-based 2D RF pulses, based on a rasterized excitation using Cartesian and spiral trajectories. In both cases, the RF pulse was designed in analogy with a 1D frequency-swept considerations made earlier; i.e., by defining the desired trajectory first in k-space, $\mathbf{k}(t)$, and applying an RF pulse with a phase-modulation of the form $\phi_{exc} = \frac{1}{2}\lambda||k||^2$, where λ is a constant. Such a phase modulation corresponds to a frequency modulation of the form $\omega = \lambda\dot{\mathbf{k}} \cdot \mathbf{k} = \gamma\mathbf{G} \cdot \lambda\mathbf{k}$, where the variable $\mathbf{r} = \lambda\mathbf{k}$ can be identified as the trajectory along which the spins are excited during the SPEN 2D pulse. These relations can be visualized clearly for the blipped Cartesian trajectory in Fig. 6a: in this case each subpulse along the "fast" x-axis becomes a chirped RF with parameters corresponding to its suitably signed ($+G_{e,x}$ or $-G_{e,x}$) excitation gradient and endowed with the desired amplitude profile, whereas increments along the "slow" y-axis are accounted by G_y "blips" and discretized amplitude/phase factors akin to those described

(a) Transverse magnetization - Hybrid 2D 90° pulse (*sinc* along k_x, uniform along y).

(b) Transverse magnetization - Hybrid 2D 90° pulse and continuous 180° chirp pulse

Fig. 5. Magnetization excited by a hybrid 2D pulse, illustrated with Bloch simulations. The magnitude and real part of the transverse magnetization is shown in (a) for a hybrid 2D pulse with $N = 150$ subpulses that sweeps over a region of interest of length ROI_y with a time-bandwidth product $Q = 100$. The waveform of the hybrid 2D pulse consists of a train of $sinc$ subpulses with a phase and amplitude given by that of the discretized chirp pulse. (b) Results for the same hybrid 2D pulse followed by a refocusing chirp pulse that sweeps over the same ROI_y in half the duration and with the same gradient amplitude. The 180° pulse was surrounded with crusher gradients and an additional gradient lobe of area $-G_eT_e/2$ (cf. Fig. 3a), leading to cancelations of both the quadratic and linear phase distortions. The two parallel lines of excited magnetization in (b) correspond to non-ideal transition regions of the refocusing pulse, and their contribution to the signal is suppressed with crusher gradients.
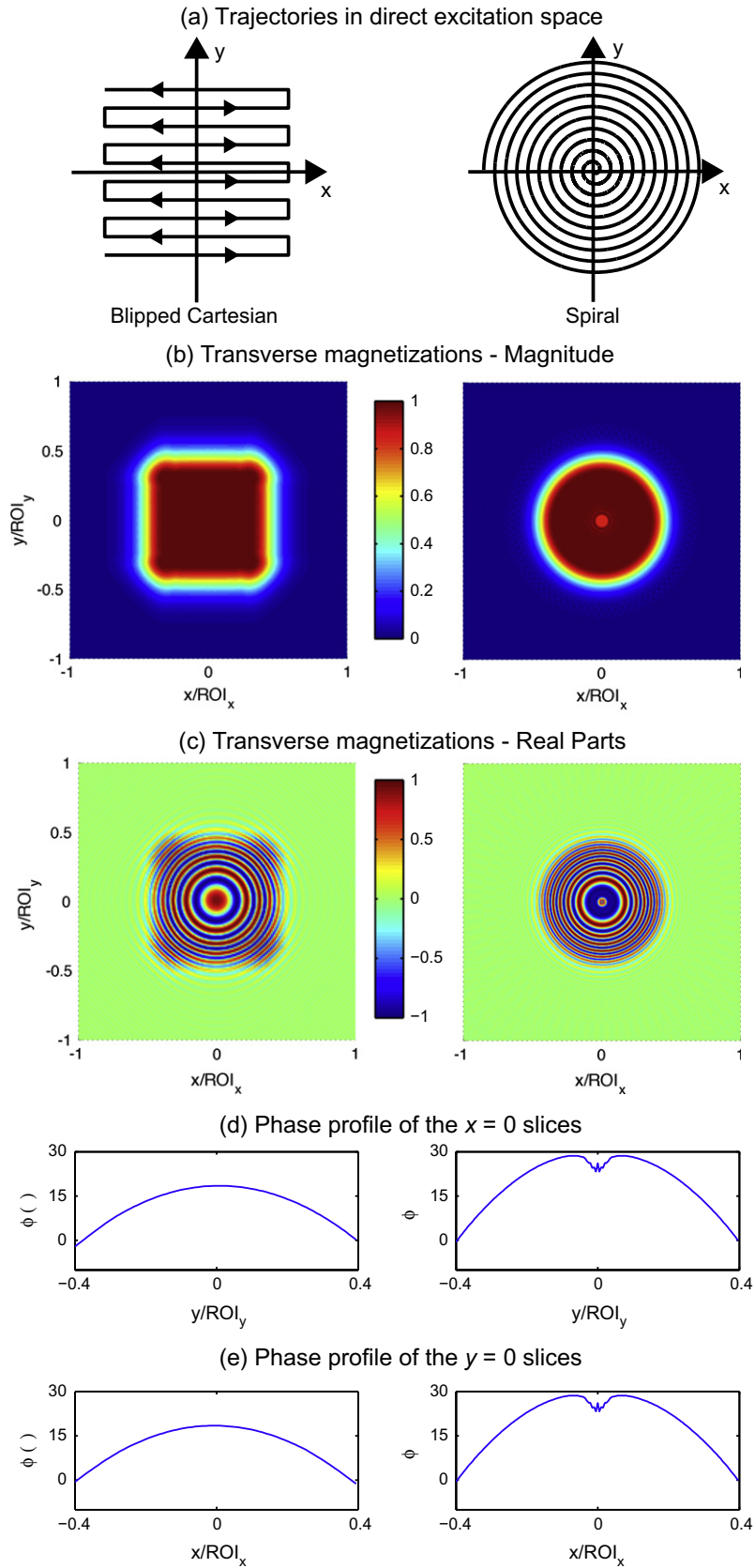
Fig. 6. Magnetization excited by a purely SPEN 2D pulse using a blipped Cartesian (left) or a spiral (right) trajectory, illustrated with Bloch simulations. The trajectory followed during excitation in a fully direct space is shown in (a). The magnitude and the real part of the transverse magnetization excited by the pulse are shown in (b and c), respectively. An additional gradient lobe is used to remove the linear phase. Panels (d and e) show the phase profile of the transverse magnetization for slices $x = 0$ and $y = 0$, respectively. The pulses have a time-bandwidth product $Q = 40$ and $N_e = 80$, where N_e is the number of lines for the blipped Cartesian and the number of turns for the spiral trajectory.

above for the hybrid 2D (y/k_x) pulse. Notice that due to this discretization procedure, the various sideband-related arguments mentioned for the hybrid case are also relevant here.

The sequential excitation of the spins along a spiral trajectory can be understood in a similar manner. For an Archimedean spiral with N turns and total duration T, depicted on the right-hand side of Fig. 6b, the k-space trajectory can be written:

$$k_x = \gamma G_0 t \cos(\omega_G t), \quad k_y = \gamma G_0 t \sin(\omega_G t), \tag{9}$$

where G_0 is a constant and a constant angular velocity has been used for simplicity. This results in a demand for the synthesis of a quadratic RF excitation phase

$$\phi = \frac{1}{2} \gamma G_0 v_0 t^2, \tag{10}$$

where v_0 is a constant representing an "average velocity" with which points being addressed at a given time move away from the center. The sequential excitation of the spins then occurs along the trajectory:

$$r_x = v_0 t \cos(\omega_G t), \quad r_y = v_0 t \sin(\omega_G t). \tag{11}$$

The excitation mechanism in this spiral case is in fact similar to that of the blipped Cartesian case: each turn of the spiral corresponds to a subpulse that sweeps continuously over the angular variable θ, while a discrete sweep over the variable r occurs over consecutive arms. Notice that the total diameter of the excited disk will then be given by $2R_X = 2Tv_0$, which acts as an "effective ROI" for such spiral excitations. Indeed, as in the 1D case, the use of a discrete number N of spiral turns implies that "excitation sidebands" will be generated in an outward radial fashion. Avoiding overlap of such concentric rings with the region of interest $2R_X$ places an upper bound on the gradient strength to be used
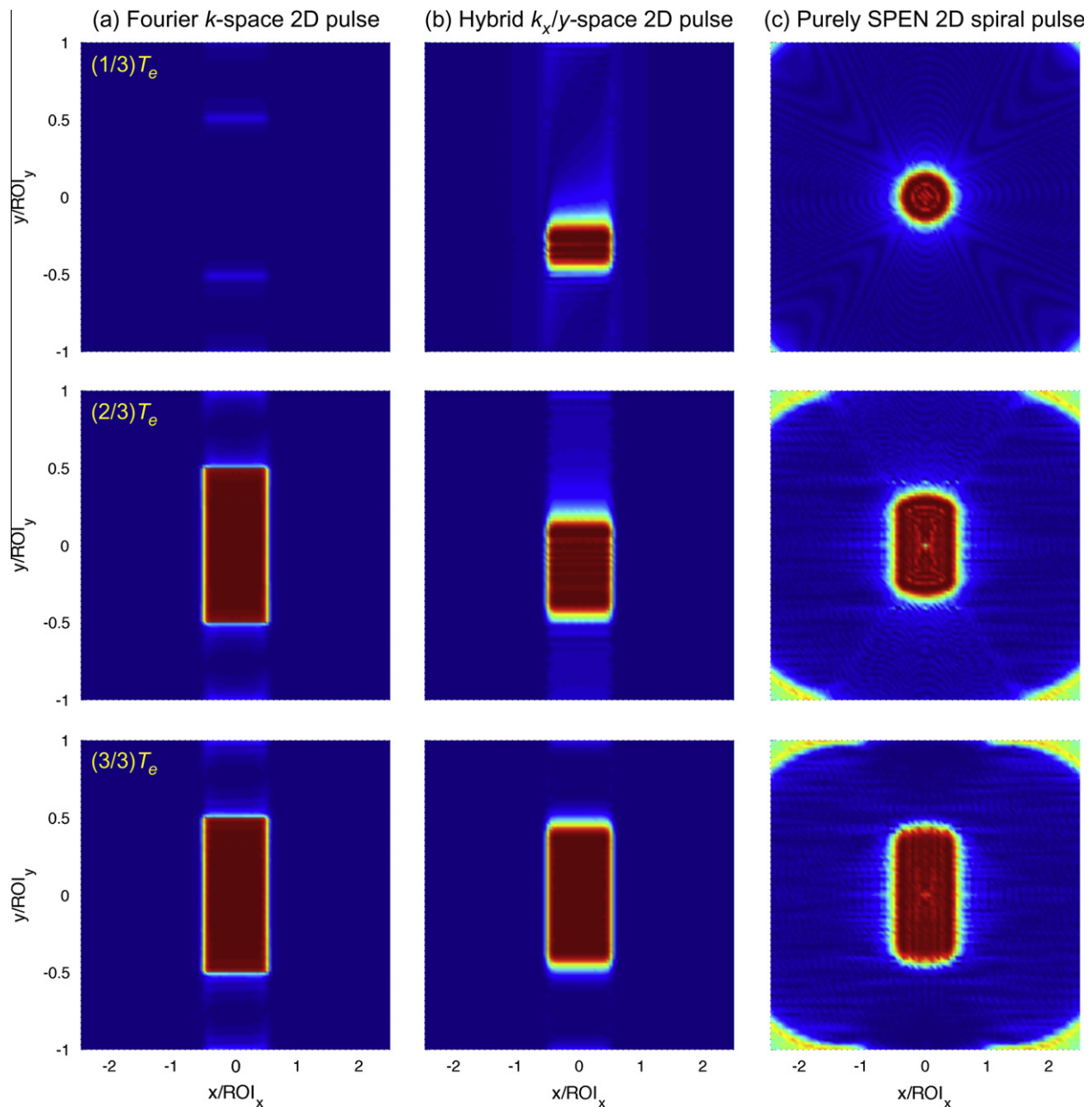
Fig. 7. Time evolution of excited transverse magnetizations during a Fourier 2D pulse (a), a hybrid 2D pulse (b) and a purely SPEN 2D spiral pulse (c), illustrated with Bloch simulations. The three pulses excite a rectangular region of interest. The magnitudes of the transverse magnetizations are shown for $t = T_e/3$, $2T_e/3$ and T_e, where T_e is the total duration of the pulse. A blipped Cartesian trajectory with $N_e = 150$ lines is used for the Fourier and the hybrid pulse, with a time-bandwidth product in the slow dimension of $Q = 100$ and $sinc$ subpulses in the fast dimension. For the SPEN pulse, a spiral with $N_e = 150$ turns and a time-bandwidth product of $Q = 100$ is used.
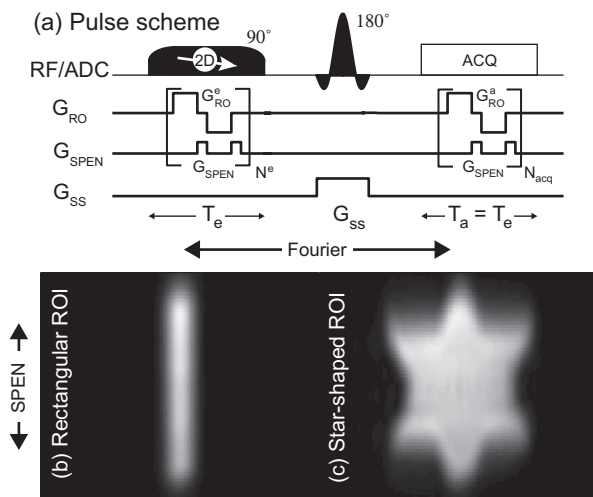
$$G_0 < \frac{2\pi N}{\gamma 2 R_X T}. \tag{12}$$

This constraint is akin to the one stated in Eq. (6) for the 1D discrete chirped excitation case. Similarly, a time-bandwidth product can be defined as $Q = 2T_e G_0 R_X$.

To conclude these considerations, it is enlightening to compare the time progression with which k-space, hybrid k/r-space and the purely-SPEN spiral pulses just treated, will excite an arbitrary rectangular shape in two dimensions. Presented as Supplementary material is an animated version of these events for a simple shape; Fig. 7 summarizes shots taken 33%, 66% and 100% throughout the course of each of these pulses. These plots evidence that whereas a classic k-space pulse excites the high-frequency and subsequently all gross features of the shape rapidly, and then invests a substantial part of the conclusion of pulse to sculpt the finer features globally, the spatially encoded pulses literally rasterize the excitation sculpting throughout the course of their frequency sweeps.

3. Methods

Experiments assaying the various considerations of the previous Section were carried out, focusing in particular on examining the performance of the hybrid 2D pulse vis-à-vis its classic k-space counterpart. These data were collected at 7 T on a Varian VNMRS 300/89 vertical-bore microimaging system (Varian associates, Palo Alto, CA) using a Millipede® probe. In all experiments a water tube of 22 mm inner diameter was used as a phantom, on which either single-scan SPEN or multi-scan spin-echo images were obtained after applying a selective 2D excitation. The generation of all RF and gradient waveforms needed to carry out these 2D pulse comparisons were written in Matlab® (The Mathworks, Natick, MA), and then exported into the NMR scanner where they were clocked out with 4 µs dwells. Data

processing was also performed off-line using custom-written Matlab routines.

The specific experimental implementations that were tested employed the sequences shown in Figs. 8a and 9a. A central refocusing 180° pulse was used to select a slice of 4 mm thickness, with phase-encoding and prephasing gradients played on both sides of this pulse, simultaneously with crusher gradients. During acquisition, the readout dimension was monitored with a 250 kHz bandwidth. A detailed description of each RF pulse is given in the figure captions. When comparing the performance of the k-space vs. the hybrid 2D pulses a flyback design was used for both cases; i.e., RF was only played during odd k-lines (positive gradient of the zig-zag) in order to avoid timing imbalances. Such timing errors are most likely due to eddy-currents, which are not fully compensated on microimaging vertical hardware. In no case were relaxation effects taken into account in the design of the RF waveforms.
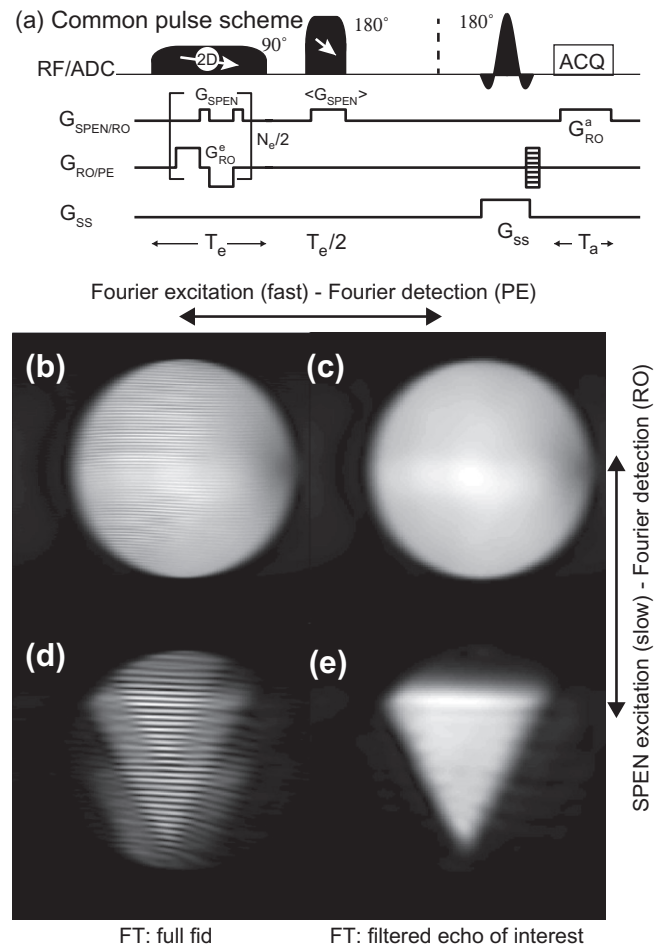
Fig. 9. Conventional 2D spin-echo images obtained after a discretized 1D excitation chirp pulse (b and c) or a hybrid 2D excitation pulse (d and e) – followed in both cases by a continuous refocusing chirp pulse – illustrating how undistorted ROIs can be recovered despite the presence of strongly overlapping excitation sidebands. The pulse sequence is shown in (a). Excitation chirp pulses were composed of N_e = 100 (b and c) or 50 (d and e) subpulses, with a duration of T_e = 20.4 ms, swept over a ROI = 3 cm with a time-bandwidth product Q = 200. A gradient G_{RO} = 10 kHz mm^{-1} was used during these subpulses, and their amplitudes were chosen to operate in the linear regime. The excitation results were imaged by spin-echo MRI with 256 × 32 points and a field of view of 3 × 3 cm². The signal consists of several echoes along the readout dimension; images (b and d) were obtained by Fourier transforming the full signal in both dimensions after zero-filling to 256 × 128. By contrast, images (c and e) were obtained by filtering, respectively, 100 and 50 points centered on the echo that correspond to the targeted ROI, zero-filling to 128 × 128 points, and 2D FT.

Fig. 8. Single-scan 2D SPEN images obtained after applying hybrid 2D pulses that excite either rectangular (b) or star-shaped (c) ROIs. The pulse sequence is shown in (a), with RO, SPEN and SS denoting orthogonal gradients applied along the read-out ("x"), SPEN ("y") and slice-select ("z") directions. The 2D pulse had N_e = 70 subpulses, a duration of T_e = 30.8 ms and swept over ROI$_y$ = 20 mm with a time-bandwidth product Q = 50 in the slow dimension. The waveform was obtained by FT of the targeted pattern along the fast dimension, and by adjusting the phase and amplitude of each subpulse according to that of a discretized chirp pulse. A gradient G_{RO} = 10 kHz mm^{-1} was used during the subpulses. 70 × 70 points were acquired in a single scan in a total time of T_a = 30.8 ms. ROI$_x$ was 2.5 cm in the readout dimension. Following suitable rearrangement the signal was FT'd along the RO and super-resolved along the SPEN dimension.

4. Results and discussion

4.1. Hybrid 2D excitations and single-scan 2D SPEN imaging

One of the features associated to selective 2D excitations with hybrid pulses is the fact that the phase imparted will contain a quadratic dependence along the "slow" dimension. This makes such pulses well suited to implement a SPEN-based detection; Fig. 8b shows a 2D image obtained in such way and in a single-scan: a hybrid 2D pulse with all the subpulses along the "fast" dimension made of identical $sinc$ profiles was applied, and the ensuing excitation then monitored using single-scan 2D SPEN MRI. The intrinsic resolution of these images was also enhanced by use of a super-resolution algorithm [42], and the acquisition was timed in order to record the full pseudo-echo in a fully refocused manner [26]. As explained earlier this SPEN NMR image does not require FT along the spatially encoded direction – only along the read-out axis. The rectangular regions selectively excited by the $sinc$ profiles are clear; notice as well that since parameters were chosen such that the excitation sidebands fell outside the sample along the "slow" axis, only the center ROI was imaged.

This simple example suggests that hybrid 2D pulses could be used to add slice selectivity to existing SPEN imaging sequences. This option was explored in Ref. [47], albeit with a different approach based on using profiles that could also be obtained by suitable intersection of two 1D selectively excited regions. The 2D hybrid SPEN pulse, by contrast, can also excite complex shapes that do not fulfill this simple property. This is illustrated in Fig. 8c, which shows the excitation of a star-shaped region and its subsequent imaging with a single-scan SPEN sequence. Notice that, being a hybrid 2D pulse, the RF waveform that leads to this profile was not obtained as the 2D Fourier transform of the region of interest. Instead, each subpulse is taken as a 1D Fourier transform of the corresponding line in the targeted region, and the frequency sweep along the "slow" dimension is then obtained by an overall phase modulation of the train of subpulses.

For a given excitation pattern and a given bandwidth, the power deposition for a SPEN-based and for a Fourier-based 2D pulse will be comparable. This reflects the fact that modulating a transverse magnetization with a quadratic-phase does not affect the energy required to excite it (see, e.g., Ref. [29]). Sequential excitation using a frequency-sweep, however, leads to a decrease of the maximum RF amplitude of a hybrid 2D pulse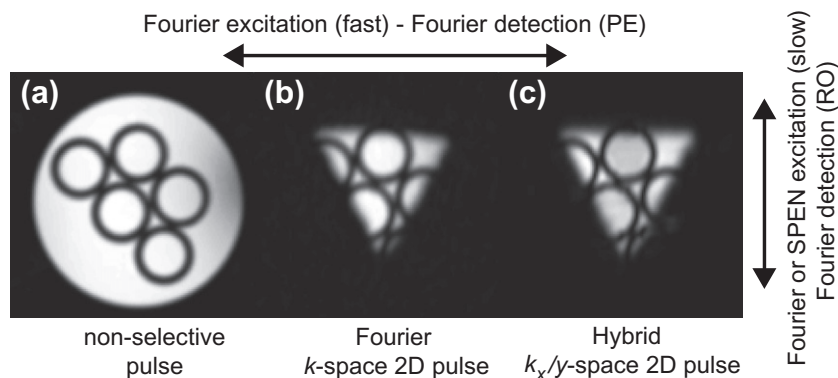 compared to a Fourier-based 2D pulse. SPEN-based 2D pulses should thus have the same compatibility with the SAR requirements of in $vivo$ imaging as conventional 2D pulses.

4.2. Fourier imaging: hybrid 2D pulses incorporating a quadratic phase refocusing

While the SPEN MRI experiment benefits in a natural way from the quadratic phase imparted by the hybrid 2D pulses just described, this pattern is not well suited for conventional k-space imaging. As discussed above, the use of a refocusing 180° chirp pulse can remove such a quadratic phase. Besides enabling conventional imaging, this adiabatic sweep opens the possibility to separate the contribution of the main ROI from that of undesirable excitation sidebands at an acquisition stage (Paragraph 2.2). This self-unfolding process is illustrated in Fig. 9 for both a discretized 1D chirp pulse exciting the full 22 mm diameter sample (panels b and c), and for a hybrid 2D pulse sculpting a triangle within this sample (panels d and e). The time-bandwidth product of these discretized chirp pulses was chosen to be ca. three times larger than the number of subpulses, and the RF intensities were adjusted to remain in the linear excitation regime of the pulses. As a result of this the imaging signals consisted of three well-separated echoes, with each echo corresponding to a center/side-band. FT of the entire signal thus yields an interfering sum of multiple folded bands along the "slow" dimension (Fig. 9, left-hand panels). However, if only a selected echo is transformed along the lines described in Fig. 3, undistorted images of the ROIs can be recovered (Fig. 9, right-hand panels).

Fig. 10 complements these tests with spin-echo images of a non-uniform phantom, obtained after exciting it with either a non-selective pulse, a k-based 2D-selective excitation, or an analogous SPEN-/k-based hybrid pulse. It can be seen that the internal features, ring-like structures in this example, are similarly resolved in the region of interest for all types of excitations: the main difference between the images afforded by conventional and SPEN-based 2D pulses arises from the higher robustness of the latter to field inhomogeneities. In general, this confirms that SPEN-based forms of multidimensional excitation is not expected to interfere with image quality for a given field of view and number of acquired points.

Although the unfolding/filtering procedure requires operating in a linear regime that may impose a price in terms of sensitivity,

Fourier excitation (fast) - Fourier detection (PE)

Fourier or SPEN excitation (slow) Fourier detection (RO)

(a)   (b)   (c)

non-selective   Fourier   Hybrid
pulse k-space 2D pulse k_x/y-space 2D pulse

Fig. 10. Conventional 2D spin-echo images obtained on a phantom consisting of five small tubes within a larger tube, using (a) a non-selective pulse, (b) a triangle-sculpting 2D pulse based on a Fourier k-space design, and (c) a similar shape but obtained using the pulse scheme in Fig. 8a, combining a hybrid 2D SPEN pulse and a refocusing 180° chirp. The hybrid 2D pulse had a duration T_e = 16.4 ms, N_e = 32 subpulses and swept over a ROI = 1.7 cm in the slow dimension with a time-bandwidth product Q = 93. The Fourier 2D pulses had the same duration, number of subpulses, and ROI; its slow-dimension bandwidth was 4 times smaller than that of the hybrid 2D pulse. The bandwidth in the fast dimension was identical for both pulses and arose from a G_{RO} = 10 kHz mm^{-1} gradient. The excitation results were imaged by spin-echo MRI with 128 × 64 points and a field of view of 2.5 × 2.5 cm. For (b and c), images were obtained by filtering 50 points centered on the echo that corresponds to the targeted ROI, zero-filling to 128 × 128 points, and 2D FT.

it also makes it possible to use more intense gradients in the "slow" dimension of a multidimensional pulse. Fig. 11 illustrates this by showing how, by enabling one to play out the pulse under stronger gradient strengths, this sideband-unfolding approach can reduce the distortions that field inhomogeneities will otherwise impart on excited ROIs. This figure compares the shaped patterns that will be excited by conventional Fourier-based and by hybrid 2D pulses, whose total duration, number of intervening subpulses, and patterns/sizes of the addressed regions, are set equal. The gradient amplitudes used along the "slow" dimension, however, were set differently: for the Fourier case this gradient was set to G_{max}, i.e. to the maximum gradient strength that allows one to operate the pulse without any overlap between the region of interest and the excitation sidebands (Eq. (4)). For the hybrid 2D pulse, the gradient amplitude was set along this axis as $4 * G_{max}$, and the sideband-filtering approach was used to retrieve solely the signal elicited by the central ROI. As can be seen from the data the shapes excited by the k-space-based 2D pulse becomes highly distorted when an overall inhomogeneity of about 200 Hz is deliberately introduced. By contrast, the pattern excited by the hybrid 2D pulse shows a much more limited distortion. Thus, despite certain drawbacks such as a longer echo time, this self-unfolding approach could be useful to achieve accurate pattern-shaping in a single scan – including 3D spatial patterns and/or 2D spatial/1D spectral patterns that would normally demand pulses on the order of 10 ms susceptible to distortions even under optimal shimming conditions. Although the gradient amplitude is increased in this approach, the power deposition does not increase, because the overall excitation sculpting process still remains in the linear regime. Further improvements could arise from incorporating into this strategy the use of parallel transmitters, or by sculpting the excitation in multiple scans. It should also be noted that the choice of the readout and phase-encoding dimensions for the slow and fast dimensions of the 2D selective excitation, respectively, is not the only possible alternative. This choice was here made to obtain an image of the excited region and illustrate the self-unfolding mechanism; other possibilities include using frequency-swept pulses along the phase-encoding or the slice-selecting dimensions. Some of these options could benefit even further from the self-unfolding procedure hereby used, since the presence of additional echoes limits the resolution in the frequency-swept dimension. When this dimension is imaged there is a tradeoff between the number of subpulses in the discretized chirp pulse and the achievable resolution; such compromise may be avoided in the other dimensions. Also worth noting is the potential of the kind of 2D pulses hereby introduced in sequences aimed at localized spectroscopy. Examples of these various features will be presented in upcoming studies.

5. Conclusion

This study introduced a variety of one- and multi-dimensional pulse shaping strategies, which operate in a direct rather than in the usual reciprocal space. By extending and exploiting k-space concepts pulses containing new, attractive aspects in terms of both their shaping performance and robustness, could be designed. If
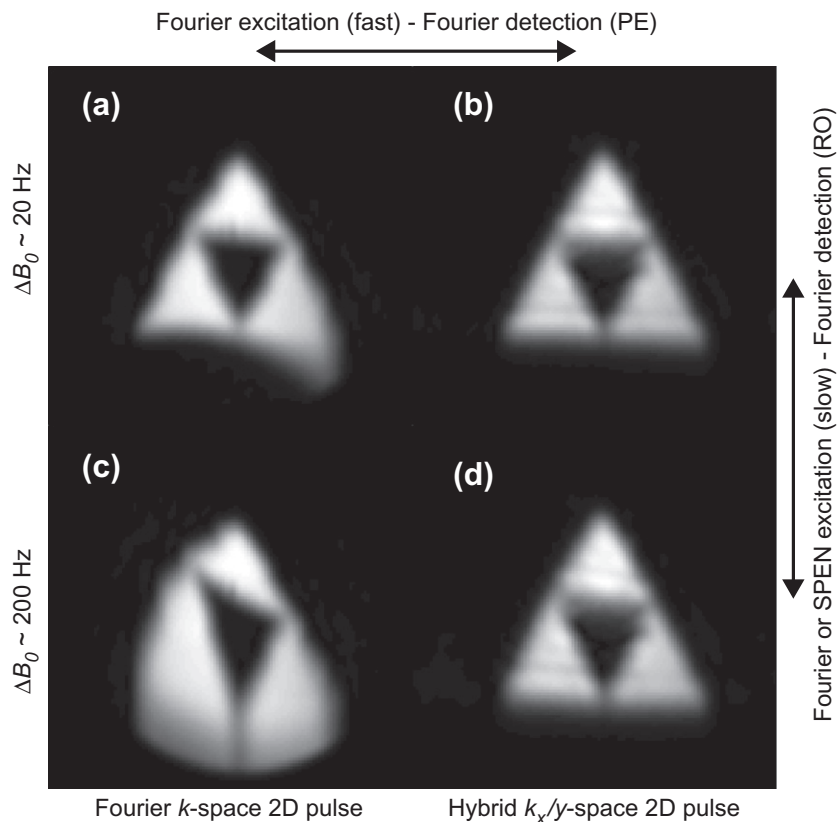
Fig. 11. Conventional 2D spin-echo images obtained after a Fourier 2D pulse (a and c) and the combination of a hybrid 2D pulse and a refocusing chirp pulse (b and d) are executed, in the presence of small (∼20 Hz, a and b) or large (∼200 Hz, c and d) field inhomogeneities. The pulse sequence is shown in Fig. 8a. The hybrid 2D pulse had a duration T_e = 16.4 ms, N_e = 32 subpulses and swept over a ROI = 1.7 cm in the slow dimension with a time-bandwidth product Q = 93. The Fourier 2D pulses had the same duration, number of subpulses, and ROI; its slow-dimension bandwidth was four times smaller than that of the hybrid 2D pulse. The bandwidth in the fast dimension was identical for both pulses and arose from a G_{RO} = 10 kHz mm^{-1} gradient. The excitation results were imaged by spin-echo MRI with 256 × 64 points and a field of view of 2.5 × 2.5 cm. Images were obtained by filtering 50 points centered on the echo that corresponds to the targeted ROI, zero-filling to 128 × 128 points, and 2D FT.

operated in their most basic fashion, the 2D sculpting achieved by these direct-space RF pulses leads to a quadratic phase that makes the excited ROIs ideally suited to SPEN-based NMR imaging strategies. The new 2D pulses can also be used within the context of conventional Fourier imaging, if post-excitation refocusing pulses are employed to remove the quadratic phase imparted at the excitation stage. The combination of the SPEN pulses with these post-excitation 180° sweeps leads to an interesting unfolding property, whereby excitation sidebands can be easily distinguished and filtered from a central ROI being targeted. This enables one to employ larger excitation gradients upon imprinting the desired spatial pattern along the "slow" axis, a feature that can be exploited to provide a higher robustness against field inhomogeneities and/or chemical shift misregistrations than what usual characterizes these relatively long and delicate pulses. Although the examples presented here only focused on simple phantoms, they illustrate the potential carried by these approaches in the design of spatial or spatial/spectral sculpting strategies by means of multidimensional RF pulses.

Acknowledgments

Appendix A. Supplementary material

Supplementary data associated with this article can be found, in the online version, at http://dx.doi.org/10.1016/j.jmr.2012.10.010.

References

[1] R. Freeman, Shaped radiofrequency pulses in high resolution NMR, Prog. Nucl. Magn. Reson. Spectrosc. 32 (1998) 59–106.
[2] R. Freeman, Spin Choreography, Oxford University Press, Oxford, 1998.
[3] M.A. Bernstein, K.F. King, X.J. Zhou, Handbook of MRI Pulse Sequences, Academic Press, New York, 2004.
[4] R.A. de Graaf, In vivo NMR Spectroscopy, Wiley, Chichester, 2007.
[5] Q. Qin, J.C. Gore, M.D. Does, M.J. Avison, R.A. de Graaf, 2D arbitrary shape-selective excitation summed spectroscopy (ASSESS), Magn. Reson. Med. 58 (2007) 19–26.
[6] W. Weber-Fahr, M.G. Busch, J. Finsterbusch, Short-echo-time magnetic resonance spectroscopy of single voxel with arbitrary shape in the living human brain using segmented two-dimensional selective radiofrequency excitations based on a blipped-planar trajectory, Magn. Reson. Imaging 27 (2009) 664–671.
[7] J. Snyder, M. Haas, J. Hennig, M. Zaitsev, Selective excitation of two-dimensional arbitrarily shaped voxels with parallel excitation in spectroscopy, Magn. Reson. Med. 67 (2012) 300–309.
[8] A.Z. Lau, A.P. Chen, R.E. Hurd, C.H. Cunningham, Spectral–spatial excitation for rapid imaging of DNP compounds, NMR Biomed. 24 (2011) 988–996.
[9] Y. Zur, Design of improved spectral–spatial pulses for routine clinical use, Magn. Reson. Med. 43 (2000) 410–420.
[10] V.A. Stenger, F.E. Boada, D.C. Noll, Three-dimensional tailored RF pulses for the reduction of susceptibility artifacts in t_2^*-weighted functional MRI, Magn. Reson. Med. 44 (2000) 525–531.
[11] S. Saekho, F.E. Boada, D.C. Noll, V.A. Stenger, Small tip angle three-dimensional tailored radiofrequency slab-select pulse for reduced b_1 inhomogeneity at 3 T, Magn. Reson. Med. 53 (2005) 479–484.
[12] C. Yang, W. Deng, V. Alagappan, L.L. Wald, V.A. Stenger, Four-dimensional spectral–spatial RF pulses for simultaneous correction of b_1^+ inhomogeneity and susceptibility artifacts in t_2^*-weighted MRI, Magn. Reson. Med. 64 (2010) 1–8.
[13] P.A. Bottomley, C.J. Hardy, Two-dimensional spatially selective spin inversion and spin-echo refocusing with a single nuclear-magnetic-resonance pulse, J. Appl. Phys. 62 (1987) 4284–4290.
[14] J. Pauly, D. Nishimura, A. Macovski, A k-space analysis of small-tip-angle excitation, J. Magn. Reson. 81 (1989) 43–56.
[15] C.H. Meyer, J.M. Pauly, A. Macovski, D.G. Nishimura, Simultaneous spatial and spectral selective excitation, Magn. Reson. Med. 15 (1990) 287–304.
[16] S. Rieseberg, J. Frahm, F. Finsterbusch, Two-dimensional spatially-selective RF excitation pulses in echo-planar imaging, Magn. Reson. Med. 47 (2002) 1186–1193.
[17] C.Y. Yip, J.A. Fessler, C.N. Douglas, Iterative RF pulse design for multidimensional, small-tip-angle selective excitation, Magn. Reson. Med. 54 (2005) 908–917.
[18] S. Ljunggren, A simple graphical representation of Fourier-based imaging methods, J. Magn. Reson. 54 (1983) 338–343.
[19] D.B. Twieg, The k-trajectory formulation of the NMR imaging process with applications in analysis and synthesis of imaging methods, Med. Phys. 10 (1983) 610–621.
[20] J. Hennig, M. Hodapp, Burst imaging, Magma 1 (1993).
[21] I.J. Lowe, R.E. Wysong, Dante ultrafast imaging sequence (DUFIS), J. Magn. Reson. B 101 (1993) 106–109.
[22] R. Chamberlain, J.-Y. Park, C. Corum, E. Yacoub, K. Ugurbil, C.R. Jack Jr., M. Garwood, Raser: A new ultrafast magnetic resonance imaging method, Magn. Reson. Med. 58 (2007) 794–799.
[23] Y. Shrot, L. Frydman, Spatially encoded NMR and the acquisition of 2D magnetic resonance images within a single scan, J. Magn. Reson. 172 (2005) 179–190.
[24] A. Tal, L. Frydman, Spatial encoding and the single-scan acquisition of high definition MR images in inhomogeneous fields, J. Magn. Reson. 182 (2006) 179–194.
[25] M.E. Meyerand, E.C. Wong, A time encoding method for single-shot imaging, Magn. Reson. Med. 34 (1995) 618–622.
[26] N. Ben-Eliezer, Y. Shrot, L. Frydman, High-definition, single-scan 2D MRI in inhomogeneous fields using spatial encoding methods, Magn. Reson. Imaging 28 (2010) 77–86.
[27] J.G. Pipe, Spatial encoding and reconstruction in MRI with quadratic phase profiles, Magn. Reson. Med. 33 (1995) 24–33.
[28] A. Tal, L. Frydman, Single-scan multidimensional magnetic resonance, Prog. Nucl. Magn. Reson. Spectrosc. 57 (2010) 241–292.
[29] D. Kunz, Use of frequency-modulated radiofrequency pulses in MR imaging experiments, Magn. Reson. Med. 3 (1986) 377–384.
[30] D. Kunz, Frequency-modulated radiofrequency pulses in spin-echo and stimulated-echo experiments, Magn. Reson. Med. 4 (1987) 129–136.
[31] J.G. Pipe, Analysis of localized quadratic encoding and reconstruction, Magn. Reson. Med. 36 (1996) 137–146.
[32] J.M. Bohlen, M. Rey, G. Bodenhausen, Refocusing with chirped pulses for broad-band excitation without phase dispersion, J. Magn. Reson. 84 (1989) 191–197.
[33] E. Kupce, R. Freeman, Adiabatic pulses for wide-band inversion and broad-band decoupling, J. Magn. Reson. A 115 (1995) 273–276.
[34] G.A. Morris, R. Freeman, Selective excitation in Fourier-transform nuclear magnetic-resonance, J. Magn. Reson. 29 (1978) 433–462.
[35] D. Idiyatullin, C. Corum, S. Moeller, M. Garwood, Gapped pulses for frequency-swept MRI, J. Magn. Reson. 193 (2008) 267–273.
[36] D.G. Norris, P.J. Koopmans, R. Boyacioglu, M. Barth, Power independent of number of slices (pins) radiofrequency pulses for low-power simultaneous multislice excitation, Magn. Reson. Med. 66 (2011) 1234–1240.
[37] J.Y. Park, L. DelaBarre, M. Garwood, Improved gradient-echo 3D magnetic resonance imaging using pseudo-echoes created by frequency-swept pulses, Magn. Reson. Med. 55 (2006) 848–857.
[38] S.F. Keevil, Spatial localization in nuclear magnetic resonance spectroscopy, Phys. Med. Biol. 51 (2006) R579–R636.
[39] J.-Y. Park, M. Garwood, Spin-echo MRI using pi/2 and pi hyperbolic secant pulses, Magn. Reson. Med. 61 (2009) 175–187.
[40] P. Balchandani, M.M. Khalighi, G. Glover, J. Pauly, D. Spielman, Self-refocused adiabatic pulse for spin echo imaging at 7 T, Magn. Reson. Med. 67 (2012) 1077–1085.
[41] M.G. Busch, F. Finsterbusch, Eliminating side excitations in propeller-based 2D-selective RF excitations, Magn. Reson. Med. (2012).
[42] N. Ben-Eliezer, M. Irani, L. Frydman, Super-resolved spatially encoded single-scan 2D MRI, Magn. Reson. Med. 63 (2010) 1594–1600.
[43] L.P. Panych, K. Oshio, Selection of high-definition 2D virtual profiles with multiple RF pulse excitations along interleaved echo-planar k-space trajectories, Magn. Reson. Med. 41 (1999) 224–229.
[44] S. Conolly, J. Pauly, D. Nishimura, A. Macovski, 2-Dimensional selective adiabatic pulses, Magn. Reson. Med. 24 (1992) 302–313.
[45] J. Pauly, D. Spielman, A. Macovski, Echo-planar spin-echo and inversion pulses, Magn. Reson. Med. 29 (1993) 776–782.
[46] J.M. Pauly, B.S. Hu, S.J. Wang, D.G. Nishimura, A. Macovski, A 3-dimensional spin-echo or inversion pulse, Magn. Reson. Med. 29 (1993) 2–6.
[47] N. Ben-Eliezer, L. Frydman, Spatiotemporal encoding as a robust basis for fast three-dimensional in vivo MRI, NMR Biomed. 24 (2011) 1191–1201.